



*AGU Advances*

First Revision [Accepted] of

**Decreased aviation leads to increased ice crystal number and a positive radiative effect in cirrus clouds**

Jialei Zhu<sup>1,2\*</sup>, Joyce E. Penner<sup>2\*</sup>, Anne Garnier<sup>3</sup>, Olivier Boucher<sup>4</sup>, Meng Gao<sup>5</sup>, Lei Song<sup>6</sup>, Junjun Deng<sup>1</sup>, Congqiang Liu<sup>1</sup>, Pingqing Fu<sup>1</sup>

<sup>1</sup> Institute of Surface-Earth System Science, School of Earth System Science, Tianjin University, Tianjin 300072, China

<sup>2</sup> Department of Climate and Space Sciences and Engineering, University of Michigan, Ann Arbor, MI 48109, USA

<sup>3</sup> Science Systems and Applications, Inc., Hampton, VA 23666, USA

<sup>4</sup> Institut Pierre-Simon Laplace, Sorbonne Université / CNRS, Paris, France

<sup>5</sup> Department of Geography, Hong Kong Baptist University, Hong Kong SAR, China

<sup>6</sup> Center for Monsoon System Research, Institute of Atmospheric Physics, Chinese Academy of Sciences, Beijing 100029, China

1  
2  
3  
4  
5  
6  
7  
8  
9  
10  
11  
12  
13  
14  
15  
16  
17  
18  
19  
20  
21  
22

# Decreased aviation leads to increased ice crystal number and a positive radiative effect in cirrus clouds

Jialei Zhu<sup>1,2\*</sup>, Joyce E. Penner<sup>2\*</sup>, Anne Garnier<sup>3</sup>, Olivier Boucher<sup>4</sup>, Meng Gao<sup>5</sup>, Lei Song<sup>6</sup>, Junjun Deng<sup>1</sup>, Congqiang Liu<sup>1</sup>, Pingqing Fu<sup>1</sup>

<sup>1</sup> Institute of Surface-Earth System Science, School of Earth System Science, Tianjin University, Tianjin 300072, China

<sup>2</sup> Department of Climate and Space Sciences and Engineering, University of Michigan, Ann Arbor, MI 48109, USA

<sup>3</sup> Science Systems and Applications, Inc., Hampton, VA 23666, USA

<sup>4</sup> Institut Pierre-Simon Laplace, Sorbonne Université / CNRS, Paris, France

<sup>5</sup> Department of Geography, Hong Kong Baptist University, Hong Kong SAR, China

<sup>6</sup> Center for Monsoon System Research, Institute of Atmospheric Physics, Chinese Academy of Sciences, Beijing 100029, China

Corresponding author: Joyce E. Penner ([penner@umich.edu](mailto:penner@umich.edu)) and Jialei Zhu ([zhujialei@tju.edu.cn](mailto:zhujialei@tju.edu.cn))

**Key words:** cirrus clouds, aircraft soot, COVID-19, radiative effects

23 **Abstract**

24           Travel restrictions in the wake of the COVID-19 pandemic resulted in an unprecedented  
25 decrease of 73% in global flight mileage in April-May 2020 compared to 2019. Here we examine  
26 the CALIPSO satellite observations and find a significant increase in ice crystal number  
27 concentrations (Ni) in cirrus clouds in the mid-latitudes of the Northern Hemisphere, which we  
28 attribute to an increase in homogeneous freezing when soot from aircraft emissions is reduced. A  
29 relatively small positive global average radiative effect of  $21 \text{ mW m}^{-2}$  is estimated if a decrease  
30 in aircraft traffic continues, with an average of up to  $64 \text{ mW m}^{-2}$  over the area where aviation is  
31 most active. We infer from this analysis that the worldwide adoption of biofuel blending in  
32 aircraft fuels that lead to smaller soot emissions could lead to a significant change in the  
33 microphysical properties of cirrus clouds but a rather small positive radiative effect.

34

35 **Plain Language Summary**

36           Cirrus clouds play an important role in the Earth's radiation budget. Whether soot from  
37 aircraft emission would change the property of large-scale cirrus clouds has been a critical  
38 question. We show that the unprecedented decrease in aircraft traffic as a result of the COVID-  
39 19 pandemic leads to a significant increase in ice crystal number as detected by satellite. An  
40 increase in ice crystal number and positive radiative effect is estimated using a state-of-the-  
41 science earth system model if the reduction in aviation activity continues for the foreseeable  
42 future. As adoption of blending biofuel in the aviation sector would lead to similar reductions  
43 (50~70%) of aircraft soot emissions in the future, remarkable changes in the microphysical  
44 properties of large-cirrus clouds and positive radiative effects can be expected relative to a case  
45 with no biofuel blending.

46

## 47 **1 Introduction**

48           The novel coronavirus disease that started in 2019 (COVID-19) has been spreading  
49 worldwide since the end of 2019, which has led to ~250 million infections and ~5 million deaths  
50 (Worldometers, 2021). Many countries have taken mandatory lockdown measures, such as losing  
51 businesses and factories and encouraging work-from-home, in order to curb the spread of  
52 COVID-19. In addition, countries have taken measures to reduce non-essential national and  
53 international travel via aircraft in order to reduce the risk of spreading COVID-19 in airports and  
54 aircraft cabins as well as to limit the number of cases imported from abroad (Bogoch et al.,  
55 2020a, 2020b). Even though social systems and the economy are recovering gradually in some  
56 countries where the pandemic is under control, some international borders are still partially or  
57 completely closed. As a result, global airlines have been forced to cut flights on a scale that has  
58 never been seen before. As many professionals are getting used to remote meetings and online  
59 conferences (Bavel et al., 2020), a full recovery of the airline industry may still be expected to  
60 take several years despite the ongoing vaccine roll-out on a global scale (Adrienne et al., 2020).  
61 The succession of lockdown measures during COVID-19 allows for an unprecedented test of  
62 anthropogenic influences on the environment and climate. Many studies have been conducted to  
63 examine the side effects of these lockdown measures on air quality, decreases in CO<sub>2</sub> emissions  
64 and climate responses, mostly caused by the large reduction in the consumption of fossil fuels in  
65 factories, power plants and motor vehicles (Forster et al., 2020; He et al., 2020; Huang et al.,  
66 2020; Le Quéré et al., 2020; Phillips et al., 2020; Venter et al., 2020; Yang et al., 2020).  
67 However, very few studies have explored the possible effect of aircraft flight reductions on  
68 large-scale cirrus clouds, which may also lead to climate change.

69           Aircraft field experiments have found that aviation exhaust particles may contribute to  
70 changes in the number densities and size of ice crystals in cirrus clouds (Ström & Ohlsson, 1998;

71 Urbanek et al., 2018). These changes to ice crystals would impact the ice water path, cloud  
72 cover, lifetime, and optical properties of large-scale cirrus clouds and thus determine their  
73 radiative properties. Satellite observations suggested a systematic, statistically significant  
74 increase in cirrus cloud optical thickness associated with aircraft flight tracks as well as complex  
75 changes in ice crystal effective radius in cirrus clouds associated with anthropogenic pollution  
76 (Tesche et al., 2016; Zhao et al., 2019).

77 The ice crystal number concentration ( $N_i$ ) in cirrus clouds is determined by the  
78 competition between homogeneous freezing of haze particles such as sulfate and heterogenous  
79 nucleation (i.e., the formation of ice initiated by the contact of liquid or gas phase water with a  
80 solid or amorphous particle). Heterogeneous nucleation may take place on ice nucleating  
81 particles (INPs) such as aircraft soot and dust particles (Cantrell & Heymsfield, 2005; Koop et  
82 al., 2000). Homogeneous freezing occurs when the relative humidity with respect to ice (RH<sub>i</sub>) is  
83 high (of the order of 150%), while heterogeneous nucleation requires much lower RH<sub>i</sub> (Hoose &  
84 Möhler, 2012). As a result, heterogeneous nucleation can occur in advance of homogeneous  
85 freezing in a rising air parcel, and thereby consume the limited water vapor supply, suppressing  
86 the occurrence of homogeneous freezing. Here we examine the effect of the decrease in aircraft  
87 soot emissions on large-scale cirrus clouds using a combination of remote sensing and modeling.

## 88 **2 Materials and Methods**

### 89 **2.1. Flight mileage and aircraft soot emissions**

90 The FlightRadar24 commercial database of individual flights for January-May in 2019  
91 and 2020 were used to reconstruct the daily spatial distribution (at  $1^\circ \times 1^\circ$  resolution) of air traffic  
92 and then interpolated into our model grids (at  $1.9^\circ \times 2.5^\circ$  resolution). The aircraft routes were  
93 assumed to follow great circles between the start and the end of the cruising parts of their

94 respective flights. We have assessed the difference in the aircraft routes between using the  
95 assumption of shortest (i.e., great circle) and fastest (i.e., fuel optimal) routes. For our grid  
96 resolution of  $1.9^{\circ} \times 2.5^{\circ}$  the difference is fairly small and has a negligible effect on the  
97 distribution of aviation-emitted soot. The Aviation Environment Design Tool (AEDT) data set  
98 was used to calculate aircraft soot emissions for 2006, which were developed based on the  
99 original flight tracks of each of 31 million commercial flights worldwide (Barrett et al., 2010;  
100 Wilkerson et al., 2010). The annually averaged growth rate of aircraft soot emissions over the  
101 period 2006 to 2012 is  $2.2\% \text{ yr}^{-1}$  and for 2013 to 2019 is  $5\% \text{ yr}^{-1}$  (Lee et al., 2021). The aircraft  
102 soot emission in January to May 2020 was estimated to be the emission in 2019 multiplied by the  
103 ratio of flight mileage in each grid for 2020 to that for the same month in 2019. The difference in  
104 aircraft soot emission in April/May between 2020 and 2019 is shown in Figure S1.

## 105 **2.2. CALIPSO satellite observations**

106 Observed  $N_i$  are derived from co-located observations of the Imaging Infrared  
107 Radiometer (IIR) and the Cloud and Aerosol Lidar with Orthogonal Polarization (CALIOP) lidar  
108 aboard the Cloud-Aerosol Lidar and Infrared Pathfinder Satellite Observation (CALIPSO)  
109 satellite. The retrieval technique uses the ratio,  $\beta_{\text{eff}}$ , of the effective absorption optical depths in  
110 IIR channels  $12.05 \mu\text{m}$  and  $10.6 \mu\text{m}$  and relationships established from SPARTICUS data using  
111 the  $N(D)_1 = 0$  assumption (Mitchell et al., 2018). The  $\beta_{\text{eff}}$  ratios are from the recent Version 4 IIR  
112 Level 2 track products (Garnier et al., 2020a, 2020b), which include improvements with respect  
113 to the previous Version 3 that were applied in a previous study (Mitchell et al., 2018). Following  
114 Version 3,  $N_i$  is retrieved for single-layered semi-transparent cirrus clouds with temperature at  
115 cloud base altitude colder than 238 K and cloud optical depth larger than about 0.3. The relative  
116 uncertainties in  $N_i$  retrievals vary with the relative uncertainties in COD, which increase rapidly

117 when COD is small ( $COD < 0.3$ ), so that Ni in clouds with  $COD < 0.3$  were not retrieved in this  
118 study (Mitchell et al., 2018). Since September 2016, the quality of the CALIOP data over the  
119 South Atlantic Anomaly (SAA) region is impacted by an increasing number of low energy laser  
120 shots. In order to prevent changes that would result from lower quality data since 2016 over the  
121 SAA, this region is removed from all the statistics for the full time period.

### 122 **2.3. CESM/IMPACT model**

123 We used the Community Earth System model (CESM) version 1.2.2 (refer to  
124 <http://www.cesm.ucar.edu/models/cesm1.2> for details) coupled to the University of Michigan  
125 IMPACT aerosol model with a resolution of  $1.9^\circ$  (longitude)  $\times$   $2.5^\circ$  (latitude) and 30 vertical  
126 layers to simulate aerosols and their effects on cirrus clouds. This version of the IMPACT model  
127 simulates the number and mass of pure sulfate in three modes (i.e. nucleation ( $< 5$  nm), Aitken  
128 ( $5-50$  nm) and accumulation ( $> 50$  nm)) and their interaction with the following fourteen other  
129 aerosol species/types. Sulfate is the only aerosol participating in homogeneous ice nucleation in  
130 the model. Soot from fossil fuel and biofuel burning (fSoot) is simulated in three modes with  
131 different hygroscopicity according to the number of monolayers sulfate on its surface while soot  
132 from biomass burning (bSoot) is simulated in one mode. 0.05% of fSoot with  $< 1$  monolayers of  
133 sulfate and 0.1% of fSoot coated with 1-3 monolayers of sulfate as well as 0.1% of bSoot are  
134 assumed to be effective INPs. Aircraft soot is simulated in two modes. The first mode has acted  
135 as an ice nuclei within contrails that subsequently evaporated (cSoot). The second mode which  
136 has not acted as an ice nuclei within contrails has only a small ability to act as an INP compared  
137 to the first mode and is not considered to act as an INP in the model. The soot that has already  
138 been included in contrail ice is treated as pre-activated. We assume that 100% of the pre-  
139 activated aircraft soot coated with less than 3 monolayers of sulfate can be an INP, similar to the

140 treatment in previous studies (Mahrt et al., 2019; Zhou & Penner, 2014) and consistent with field  
141 observations of dust and the treatment of dust in the model. This results in approximately 0.6%  
142 of all emitted aircraft soot that can possibly acting as an INP to form ice. The model's ability to  
143 simulate the profile of soot from fossil fuel, biofuel and aircraft emissions was evaluated by  
144 comparison with field campaigns (Figure 2 in Samset et al., 2014; Figure S15 in Zhu et al.,  
145 2019). Dust and sea salt are each carried in four separate bins with varying radii. It is assumed  
146 that dust with fewer than 3 monolayers of sulfate coating can act as an INP to form ice in the  
147 model. As noted in Penner et al. (2018), this treatment is consistent with the results of field  
148 studies (Cziczo et al., 2004; P. DeMott et al., 2003; Richardson et al., 2007). The explicit number  
149 concentration of newly formed secondary organic aerosol (SOA) in the accumulation mode  
150 nucleated from highly oxygenated organic molecules (HOMs) that form from the oxidation of  $\alpha$ -  
151 pinene is read in as a possible INP in the model. The nucleated SOA particles grow by deposition  
152 and coagulation of sulfuric acid as well as by oxidation products of isoprene,  $\alpha$ -pinene, limonene  
153 and aromatics, that are in the aerosol phase. This SOA was simulated using the version of the  
154 CESM/IMPACT model outlined in our previous studies (Zhu & Penner, 2019; Zhu et al., 2017;  
155 Zhu et al., 2019). The SOA that meets the requirements of the glass transition temperature and  
156 RHi calculated using the equations in Wang et al. (2012) is able to act an effective heterogeneous  
157 INP. Soot (i.e., aircraft, fSoot, and bSoot) as well as SOA were set to activate at an RHi of 135%  
158 (but with varying fractions, see above) while dust satisfying the sulfate coating criteria activates  
159 at 120%. The assumptions for aerosols to be effective INPs in the model are summarized in  
160 Table 1 of Penner et al., 2018.

161 The HYBRID ice nucleation scheme is used to calculate the initial ice crystal number  
162 concentration in cirrus clouds from homogeneous and heterogeneous nucleation of aerosols.



163 The HYBRID scheme combines the best features of two previous ice nucleation schemes, so that  
164 our model is able to calculate the ice number concentration change in both updrafts and  
165 downdrafts associated with a parameterization of sub-grid scale gravity waves and has a robust  
166 sensitivity to the change in aerosol number. The effect of ice nucleation within pre-existing ice in  
167 cirrus clouds is not considered in this version of model. The uncertainty associated with the  
168 assumption of no ice formation in pre-existing ice is discussed in the Supplemental Text S1.  
169 After ice nucleation, the growth and sedimentation as well as evaporation of ice crystals follow  
170 the treatment in the CESM. In addition, the changes to cirrus clouds have feedbacks as a result of  
171 changes to the radiation budget, temperature, and the formation of warm clouds, as simulated in  
172 the CESM model. The ability of CESM/IMPACT and the HYBRID ice nucleation scheme to  
173 simulate the ice crystals in cirrus clouds have been evaluated in (Penner et al., 2018; Zhu &  
174 Penner, 2020b).

175 Two cases (EX\_S1 and EX\_S2) were run to examine the influence of aircraft emissions  
176 reductions due to the COVID-19 pandemic in 2020 on cirrus clouds. In these runs, the winds  
177 were nudged towards ECMWF reanalysis data using a nudging time of 6 hours for January 2017  
178 to May 2020. The aircraft soot emissions for EX\_S1 and EX\_S2 are the same for January 2017  
179 to December 2019. The emission for EX\_S1 in 2020 is the same as the emission in 2019, while  
180 the emission for EX\_S2 in 2020 is decreased based on the reduction in aircraft mileage. The  
181 effect of the reduction in aircraft emissions due to the COVID-19 pandemic was estimated as the  
182 difference between EX\_S2 and EX\_S1 in 2020. Two cases, EX\_L1 and EX\_L2, were run to  
183 examine the influence of the assumption of a long-term reduction in aircraft flights, These were  
184 run for 6 years with winds nudged towards ECMWF reanalysis data using a nudging time of 6  
185 hours for the years 2009-2014. The data for the last five years were used for analysis. The

186 aircraft emissions in EX\_L1 are increased by 5% per year from the emissions in 2019, while the  
187 aircraft emissions in EX\_L2 are decreased from that in EX\_L1 by the ratio of flight mileage  
188 reduction in April/May 2020 compared to April/May 2019. The difference in the ice crystal  
189 number,  $N_i$ , and radiation between EX\_L2 and EX\_L1 is the long-term effect of the aircraft  
190 reductions on cirrus clouds.

### 191 **3. Results**

#### 192 **3.1. Decrease in global flight mileage due to COVID-19**

193 Global aircraft flight mileage increased by ~5% annually between 2012 and 2019 (based  
194 on global aviation fuel use) (Lee et al., 2021) due to the rapid expansion of civil aviation  
195 (SABRE, 2020). This pattern of growth was expected to continue for the next two decades  
196 before the COVID-19 outbreak according to Airbus's global market forecast (Airbus, 2019).  
197 However, this trend was terminated when international airlines stopped operating flights into and  
198 out of China in February 2020. We reconstructed the daily spatial distribution of air traffic using  
199 the FlightRadar24 commercial database of individual flights for 2019 and 2020 (Figure S2).  
200 Flights were reduced in China while flights were still slightly increased in other regions in the  
201 early stage of the pandemic (January and February 2020) compared to the same period in 2019,  
202 resulting in a 0.3% decrease in global average flight mileage (Figure S2a). Travel restrictions  
203 gradually spread over the world in March 2020 with a decrease of 26% in the global average  
204 flight mileage compared to March 2019 (Figure S2b). In April and May 2020, flights were  
205 reduced significantly all over the world and global average flight mileage was decreased by 73%  
206 compared to that for the same period in 2019, which we term the severe stage of the pandemic  
207 (Figure S2c). Here we examine the change in cirrus clouds in January-February (relative to  
208 previous years) and the change in April-May (relative to previous years).

### 209 **3.2. Increased ice crystal number detected by satellite**

210 Satellite remote sensing provides a unique method for monitoring the global distribution  
211 of cloud properties with high spatial resolution, which enables the examination of changes to  
212 cirrus clouds and climate during the lockdown period. Figure 1 shows the average and median Ni  
213 in four latitude bands ( $30^{\circ}\text{N}\sim 60^{\circ}\text{N}$ ,  $0\sim 30^{\circ}\text{N}$ ,  $30^{\circ}\text{S}\sim 0$ ,  $60^{\circ}\text{S}\sim 30^{\circ}\text{S}$ ) retrieved from CALIPSO  
214 observations (details in Section 2.2). Both the median and the average Ni were similar in  
215 January-February of 2018, 2019 and 2020. In contrast, it is evident that the median and average  
216 Ni in April-May of 2020 is higher relative to Ni for 2018 and 2019 between  $30^{\circ}\text{N}\sim 60^{\circ}\text{N}$  latitude  
217 and  $22.5^{\circ}\text{E}\sim 97.5^{\circ}\text{E}$  longitude and Ni continues to be slightly higher to about  $165^{\circ}\text{E}$ , which  
218 includes China (Figure 1, dotted black box in Panel B). This is immediately downwind of  
219 western Europe, a region with large decreases in aviation (Figure S2c). Although aviation also  
220 decreased in North America (Figure S2c), the change in Ni is not remarkable over and downwind  
221 of North America. Mountainous terrain is downwind (east) of Europe while the Atlantic Ocean is  
222 east of North America. Examination of global plots of Ni from satellite remote sensing suggests  
223 that homogeneous nucleation is most active over mountainous regions (Gryspeerd et al., 2018;  
224 Mitchell et al., 2018; Sourdeval et al., 2018) since retrieved Ni is highest over and downwind of  
225 these regions. A large eddy simulation (LES) study shows that cirrus Ni in orographic regions  
226 changes rapidly as INP concentrations increase above those for a pure homogeneous nucleation  
227 case (Joos et al., 2014). Thus, the largest changes in Ni in the  $30^{\circ}\text{N}\sim 60^{\circ}\text{N}$  latitude band may be  
228 over mountainous terrain downwind of aviation decreases.

229 Most cirrus clouds in the tropics (between  $30^{\circ}\text{S}\sim 30^{\circ}\text{N}$ ) are of convective origin (i.e.,  
230 anvil cirrus) where ice crystals are nucleated in the strong updraft below the cirrus anvil by either  
231 homogeneous or heterogeneous nucleation or ice multiplication processes (P. Lawson et al.,  
232 2017; R. P. Lawson et al., 2015), often in a mixed phase environment (Blaz Gasparini et al.,

233 2019; B. Gasparini et al., 2018). This differs greatly from cirrus conditions outside of the tropics  
234 especially during non-summer months where homogeneous and heterogeneous nucleation may  
235 compete in non-anvil (i.e. large-scale) cirrus. This competition process is much more likely to be  
236 sensitive to a change in INPs (Joos et al., 2014). Therefore, due to the different nucleation  
237 processes, changes in INP concentration are not as likely to affect cirrus Ni in the latitude band  
238 from 30°S~30°N (Figure 1C). The latitude band between 60°S~30°S is also not likely to exhibit  
239 significant changes in cirrus Ni since this latitude band experiences relatively little aviation  
240 (Figure S2). The Ni peak at ~70°W in the band from 60°S~30°S is possibly due to orographic  
241 ascent over the Andes (Gryspeerd et al., 2018; Mitchell et al., 2018).

242 Paired Student's t tests (for averages) and Mood's tests (for medians) were applied for the  
243 change in Ni in 2020 relative to 2018 and 2019 to examine the significance of changes (Table 1).  
244 The differences in the median and average Ni over all latitude bands in January-February  
245 between 2018, 2019 and 2020 were not significant at a 90% significance level. Natural variations  
246 in meteorological conditions and regular anthropogenic activities between different years within  
247 a three-year period thus do not affect large-scale cirrus clouds significantly. However, the change  
248 in both the median and average Ni concentrations over 60°S-60°N in April-May 2020 are  
249 significantly different from those in 2018, 2019 and the average of 2018 and 2019 at a >95%  
250 significance level (Table 1). The median Ni over 30°N-60°N in April-May 2020 was  
251 significantly different from that in 2018 and 2019 at a >95% significance level. The difference in  
252 the median and average Ni in April-May 2020 was also significant compared to Ni in 2018 and  
253 the average of 2018 and 2019 over the 0°-30°N latitude band at a >95% significance level. In the  
254 Southern Hemisphere (SH), only the median Ni over 60°S-30°S in April-May 2020 is  
255 significantly different from that in 2019 and the average in 2018 and 2019.

256 The median and average Ni in April-May 2020 were also compared to that in April-May  
257 over the last ten years (2010-2019). The Ni concentrations over 60°S-60°N, especially in the  
258 Northern Hemisphere (NH), in April-May 2020 were also significantly different from that in the  
259 last ten years at a >95% significance level (Table 1). The Ni anomaly over 30°N~60°N in April-  
260 May 2020 stands out from the series of Ni anomalies (after detrending) over 2010-2020 (Figure  
261 1, Panel C). The anomaly in 2013 is nearly as large as that in 2020 (14/L as opposed to 20/L).  
262 However, the increase in 2013 may be associated with the unusually cold temperatures in the  
263 upper troposphere over 30°N-60°N in April/May 2013, while the average temperature in  
264 April/May 2020 was 0.53°C higher than in April/May 2013 (Figure S3). While meteorological  
265 differences cannot be entirely excluded as an explanation for the differences in April-May 2020,  
266 the large latitude bands considered here argues against this explanation for 2020 compared to an  
267 analysis that only examined the conditions over Europe for contrail formation in 2020  
268 (Schumann et al., 2021). The Ni anomaly in April-May 2020 over other latitude bands was not  
269 evidently different from that over the last ten years (Figure 1, Panel C). In addition, the most  
270 evident increases in the observed Ni over 30°N-60°N were found over 30°E-75°E (downwind of  
271 western Europe) and 105°E-135°E (over and downwind of Asia) according to the detrended  
272 anomalies in Ni in April-May of 2010-2020 (Figure S4). As shown in Figure S2c, travel  
273 restrictions caused the largest reduction of flight mileage in the NH, especially over North  
274 America, Europe, and East and Southeast Asia, while there are much smaller influences in the  
275 SH. This may explain the significant change in Ni from CALIPSO observations over the NH but  
276 insignificant change over the SH in April-May 2020 compared to the observed Ni in previous  
277 years.

### 278 **3.3. Microphysical effects during the severe stage of COVID-19**

279 We employed model simulations to attribute the observed changes in Ni to the reduction  
280 in air traffic and to determine the effects on cirrus clouds and radiation. The emissions of SO<sub>2</sub>  
281 and black carbon in China, one of the largest emission sources over the world, were only reduced  
282 by 3~5% in April/May 2020 compared to those in the same months of 2019 (Zheng et al., 2021)  
283 while surface emissions of black carbon in Europe decreased by about 11% for January-April  
284 (Evangelidou et al., 2021). Since these emissions have a smaller efficiency for the nucleation of  
285 new ice crystals in cirrus clouds than do aircraft emissions (Section 2.3) and the reductions of  
286 these emissions are smaller than that for aircraft, we assumed that any changes in surface  
287 emissions of SO<sub>2</sub> and soot during the pandemic would have a negligible effect on cirrus clouds  
288 compared to the large changes in aircraft emissions.

289 The simulated Ni from January to May in 2018, 2019 and 2020 using the  
290 CESM/IMPACT model was evaluated using data from the CALIPSO satellite (Figure 2). The  
291 observational data is limited to ice water mixing ratios  $> 10^{-6}$  kg/kg and cloud optical depths  
292 (COD) between 0.3 and 3, so model results are restricted to only these values. When the  
293 microphysical index of the infrared imaging radiometer onboard CALIPSO is less than the  
294 sensitivity limit for measuring large crystals, Ni was assigned to the values corresponding to this  
295 sensitivity limit. As a result, the average Ni determined from CALIPSO was thought to be  
296 overestimated (see below, however). It is anticipated that the median Ni is more accurate and can  
297 be used to evaluate the model. As shown in Figure 2, the simulated median Ni was close to the  
298 observed Ni with an average bias of 21%, and was mostly within the range of the 25<sup>th</sup> and 75<sup>th</sup>  
299 percentiles of the observations. In contrast, the simulated average Ni is larger than the observed  
300 average with an overall bias of 60%. Moreover, the 75<sup>th</sup> percentile of the simulated Ni is higher  
301 than that of the observed Ni. In the model as well as observations, there are infrequent occasions

302 during which very high Ni occur as a result of high updraft velocities and/or smaller INP  
303 concentrations (Jensen et al., 2013; Penner et al., 2018). This may indicate that while the model  
304 reproduces the median Ni from CALIPSO reasonably well, there are a sufficient number of cases  
305 with very high simulated Ni that may be missed by the CALIPSO observations, thereby reducing  
306 the average CALIPSO Ni. It is likely that these are cases in which the crystals are formed by  
307 homogeneous freezing. Because the number of aerosol particles that can freeze homogeneously  
308 is much larger than the number of INPs, homogeneous freezing always leads to a much higher Ni  
309 with smaller ice crystal sizes than cases with significant heterogeneous nucleation. We infer that  
310 the CALIPSO average Ni is too low by examining the model results using CALIPSO constraints  
311 versus conditions for the model as a whole, as follows. The average Ni for the cases when  
312 homogeneous freezing occurs in the model (when constrained to the CALIPSO sampling  
313 conditions) is  $4042 \text{ L}^{-1}$ , which is almost 2 orders of magnitude larger than the average Ni from  
314 heterogeneous nucleation ( $85 \text{ L}^{-1}$ ). However, the occurrence frequency of homogeneous freezing  
315 is much lower than that of heterogeneous nucleation because of the requirement of higher  
316 supersaturations which are typically associated with larger updraft velocities. The annual average  
317 occurrence frequency of homogeneous freezing is low for the average of all cases in the model,  
318 i.e. <15% over different regions with a global average of 2.2% (Figure S5a). However, the  
319 occurrence frequency is even lower when the model results are constrained to the COD and ice  
320 water mixing ratios for the CALIPSO sampling conditions, i.e. a global average of 0.4% with  
321 <7% over different regions (Figure S5b). In addition, CALIPSO is a polar orbiting satellite  
322 which follows a sun-synchronous orbit. All the CALIPSO satellite observations were made  
323 around 0130 and 1330 local time with an average revisit period of ~16 days. As a result of both  
324 the CALIPSO sampling conditions and its polar orbit, CALIPSO may miss the small number of

325 occurrences of homogeneous freezing with high levels of Ni. Consequently, we suggest that the  
326 median Ni from CALIPSO should be used to describe the observed Ni, since this would not be as  
327 influenced as much as the average Ni as a result of CALIPSO missing some cases when  
328 homogeneous freezing occurs. Of course, our radiative forcing estimates (see below) are more  
329 sensitive to the average Ni, so these estimates cannot be evaluated using the CALIPSO  
330 observations and remain uncertain. When the CALIPSO satellite happens to see a case with  
331 homogeneous freezing, the average Ni could be significantly increased. For example, the average  
332 Ni near 37.5°E for 0-30°N in January-February of 2019 is larger than the 75<sup>th</sup> percentile value of  
333 the median, possibly because of the influence of homogeneous freezing (Figure 1). Moreover,  
334 the CALIPSO satellite has a relatively larger chance of catching the occurrence of homogeneous  
335 freezing in polar regions (Figure S5b) because of the constraints used in the CALIPSO  
336 algorithm. This might explain the increasing number of pixels with high median Ni in the  
337 observations towards polar regions (Figure S6 and Figure 12a in ref. (Mitchell et al., 2018)). In  
338 spite of the low occurrence frequency of homogeneous freezing, the high Ni with small ice  
339 crystal size caused by homogeneous freezing always dominates the annual average radiative  
340 effect of cirrus clouds. Therefore, the CALIPSO satellite observation cannot, by itself, be used to  
341 examine the radiative effect of cirrus clouds influenced by changes in aircraft flights. Rather,  
342 modeling of ice nucleation and cirrus clouds is needed.

343 We examined the effect of a decrease in aircraft flights on Ni by contrasting a simulation  
344 using the actual aviation activity in 2020 with a second simulation that assumes the same  
345 aviation activity in 2020 as in 2019. We decreased the emission of aircraft soot from 2019 to  
346 2020 by the ratio of the flight mileage in 2020 to that in 2019 in each grid. This leads to a  
347 decrease of  $0.28 \pm 0.44 \times 10^8 \text{ m}^{-2}$  in the modeled global average vertically-integrated INPs (i.e.



348 contrail-processed soot with less than 3 monolayers of sulfate) from aircraft soot during April-  
349 May 2020 (Figure S7). As a result, the global average vertically-integrated Ni during April-May  
350 2020 was increased by  $0.30 \pm 0.68 \times 10^8 \text{ m}^{-2}$  (Figure S8a), while the median vertically-integrated  
351 Ni increased by  $0.06 \pm 0.86 \times 10^8 \text{ m}^{-2}$ . The increase in the average Ni is mostly attributed to the  
352 increase of  $0.33 \pm 0.68 \times 10^8 \text{ m}^{-2}$  in the contribution of homogeneous freezing, although the Ni  
353 from heterogeneous nucleation was decreased by  $0.03 \pm 0.26 \times 10^8 \text{ m}^{-2}$  (Figure S8). The reduction  
354 of aircraft soot emissions imposes the largest effect on Ni in the tropics, especially in the western  
355 Pacific Ocean and north Indian Ocean, because of the high occurrence frequency of  
356 homogeneous freezing there (Figure S5a). Because the change in Ni has a very large standard  
357 deviation indicating that this change is not statistically significant in most regions, the radiative  
358 effects are also not statistically significant (not shown). Thus, the reduction in aviation flights  
359 over a short period such as experienced in April and May, 2020, probably does not have a large  
360 influence on global climate change, but it offers insights into cirrus processes.

361 To examine the model's ability to determine the change in Ni, Table S1 presents the  
362 calculated median change in Ni in the model when restricted to the CALIPSO conditions for the  
363 same latitude bands and cases as those shown for CALIPSO in Table 1. While most of the  
364 calculated changes in Ni for the model are not statistically significant, the difference in the  
365 median value for 30-60N between 2020 and the average of 2018 and 2019 is  $19 \text{ L}^{-1}$  while it was  
366 larger for CALIPSO ( $31 \text{ L}^{-1}$ ). For 0-30N the model differences are larger than the observations  
367 ( $16 \text{ L}^{-1}$  vs  $11 \text{ L}^{-1}$ ). It is difficult to draw conclusions from this comparison since the simulated  
368 model changes are not significant.

### 369 **3.4. Radiative effects of longer-term reductions in aviation**

370           Given the uncertainty in the duration of the pandemic as well as the uncertainty in  
371 vaccine adoption, it is very possible that a reduction in aviation activity could continue for the  
372 foreseeable future. As a thought experiment, we assumed that a reduction of aviation activity  
373 lasts for five years with the same reduction ratio of aircraft soot emissions as during April-May  
374 2020, thereby exploring the largest possible effect on large-scale cirrus clouds compared to the  
375 scenario without any pandemic. This reduction (~73%) in aircraft soot emissions is similar to the  
376 anticipated 50~70% reduction as a result of the blending of biofuels with aircraft kerosene  
377 (Moore et al., 2017). In this scenario, the annual global average column number concentration of  
378 ice crystals is increased by  $0.08 \pm 0.03 \times 10^8 \text{ m}^{-2}$  (Figure 3a). In particular, the increase in Ni is  
379 significant over  $35^\circ\text{N} \sim 75^\circ\text{N}$  in northern Eurasia and over the northern most Atlantic Ocean  
380 where air routes are frequent (Figure 3a, b). The influence of the flight reduction on Ni in the  
381 tropics results in a significant increase in Ni in the north Indian Ocean, Southeast Asia, and the  
382 Caribbean Sea together with significant decreases in some regions of the tropical Pacific Ocean  
383 (Figure 3a). The larger increases in Ni in the tropics near Asia compared to the changes in mid-  
384 latitudes of the NH are the result of the very high levels of homogeneous nucleation there (Figure  
385 S5, and Figure 2 in ref. (Zhu & Penner, 2020b)), causing larger increases in Ni when the INPs  
386 from aircraft are reduced. The decreases in Ni in some parts of the tropical Pacific appear to be  
387 associated with a decrease in homogeneous nucleation and a small increase in heterogeneous  
388 nucleation (Figure 3b) which is thought to be the result of feedbacks caused by temperature  
389 changes associated with the changes in Ni, although more work is needed to confirm this (Zhu &  
390 Penner, 2020b). The increase in Ni in the northern mid-latitudes is mostly explained by the  
391 significant increase of homogeneous freezing, although the column number concentration of ice  
392 crystals from heterogeneous nucleation is decreased due to the decrease in INPs from aircraft

393 soot (Figure S9). The decrease in INPs weakens the suppression effect of heterogeneous  
394 nucleation on homogeneous freezing leading to a significant increase in the occurrence  
395 frequency of homogeneous freezing (Figure S10). This results in an increase of  $0.14 \pm 0.04 \times 10^8$   
396  $\text{m}^{-2}$  in the global average column number concentration of ice crystals from homogeneous  
397 freezing (Figure S9). The increase in Ni has a positive effect ( $63 \pm 17 \text{ mW m}^{-2}$ ) on longwave  
398 radiation and a negative effect ( $-41 \pm 21 \text{ mW m}^{-2}$ ) on shortwave radiation (Figure 3d and Figure  
399 S11). As a result, the global annual average net radiation is increased by  $21 \pm 27 \text{ mW m}^{-2}$ , with a  
400 particularly significant increase of  $64 \text{ mW m}^{-2}$  over  $50^\circ\text{N} \sim 75^\circ\text{N}$  (Figure 3c,d). We note that the  
401 radiative effect of decreased aviation is sensitive to the concentration of other INPs (e.g. SOA as  
402 well as dust and the concentration of sulfate (Zhou et al., 2014)). Of these, we consider our  
403 treatment of SOA as an INP the most uncertain. If SOA is not included as an efficient INP, the  
404 global annual average net radiative effect of a long-term decrease in aviation increases to  $34 \pm 27$   
405  $\text{mW m}^{-2}$ , which is 62% more positive than the case reported above that included SOA as an INP  
406 (Figure S12). Moreover, the increase in average ice crystal number due to the decrease in  
407 aviation in the case excluding SOA is 19% larger than that in the case that includes SOA. In  
408 addition, excluding SOA as an INP leads to an average bias of the median Ni in comparison to  
409 CALIPSO of 37% compared to only 21% when SOA is included.

#### 410 **4. Discussion**

411 This study examines the radiative effect of the decrease in aircraft flights due to the  
412 COVID-19 pandemic and the resulting increase of Ni in large-scale cirrus clouds in the NH  
413 using a combination of remote sensing and modeling. The CALIPSO satellite data indicates that  
414 there was a significant increase in Ni in April-May 2020 over  $30^\circ\text{N} \sim 60^\circ\text{N}$  compared to previous  
415 years. The model predicted median Ni is within 21% of that measured by CALIPSO, but because

416 CALIPSO probably misses some homogeneous freezing cases with high Ni, due to the low  
417 frequency of homogeneous freezing and long revisit period of CALIPSO, the resulting average  
418 Ni is smaller than that in the model. A set of polar orbiting satellites with a higher temporal  
419 resolution or a geostationary satellite would be needed in the future to detect average changes in  
420 Ni and to examine the cases with homogeneous freezing.

421 Our model results suggest a significant increase in Ni and a positive radiative effect over  
422 most regions in the middle to high latitudes of the NH if flight restrictions last for five years.  
423 While recent theoretical treatments indicate that the INP efficiency of aircraft soot is quite small  
424 (Kärcher et al., 2021), it is not yet clear that such treatments apply to aircraft soot in the  
425 atmosphere and its effect on large-scale cirrus clouds. Had we applied such small efficiencies in  
426 the model, we would no longer fit the CALIPSO data as well as we do. It might be that the  
427 laboratory observations on which Kärcher et al. (2021) based their parameterization do not  
428 correctly represent the effects of aircraft soot on large-scale cirrus. Thus, the INP efficiency of  
429 aircraft soot that has been incorporated in contrails is possibly the dominant uncertainty in the  
430 evaluation of the effect of aircraft emissions on cirrus clouds (P. J. DeMott et al., 1999; Hoose &  
431 Möhler, 2012; Mahrt et al., 2020; Mohler et al., 2005). More targeted field measurements are  
432 needed in the future to confirm the ability of aircraft soot to act as an INP in different  
433 atmospheric conditions and as a result of contrail-processing and coating with other compounds,  
434 in order to guide the development of model parametrizations. CALIPSO observations during the  
435 flight restriction period associated with the COVID-19 pandemic verifies to some extent the  
436 effect of aircraft soot on large-scale cirrus clouds, although it is unable to determine their  
437 radiative effects. More measurements of the aircraft soot emission rate and the efficiency of

438 aircraft soot as an INP under various conditions would be useful in the future to better constrain  
439 the aircraft soot emission inventory and its radiative effects in the model.

440 Other uncertainties in the model concern the effect of coatings on INP. We note that the  
441 coating on aircraft soot by SOA could alter its ability to act as an INP, and thereby change its  
442 effect on cirrus clouds. While sulfuric acid coating decreases the ability of aircraft soot to act as  
443 an INP in the model, it is possible that coating by SOA increases its ability. The potential  
444 influence of both sulfuric and SOA coating of aircraft soot is discussed more in the Supplemental  
445 Text S2, but it is still difficult to quantify the effect of these coatings on ice nucleation. Further  
446 quantitative experiments are needed to develop an appropriate parameterization.

447 While our model does a reasonable job of explaining the increase in Ni in CALIPSO  
448 observations, other model choices might also explain this increase. In particular, aircraft contrails  
449 are known to increase cirrus clouds and, had we included the effect of pre-existing ice in the  
450 model, reductions in aircraft contrails might also increase Ni. However, an examination of high  
451 cloud fraction observed by MODIS in April and May 2020 compared to earlier years found only  
452 very small changes that were not significant (Table S2). These small changes in high cloud  
453 fraction may be the result of the change in natural cirrus clouds which would increase when  
454 contrails are removed (Bickel et al., 2020). Thus it seems that while a decrease in cloud fraction  
455 as an explanation for the increase in Ni observed by CALIPSO may be partly responsible, it may  
456 be less important than changes in Ni resulting from the decrease in aircraft soot.

457 Partial or total decarbonation of the aviation sector through blending biofuels with  
458 aviation kerosene could reduce the particle number and mass emissions by 50-70% in the future  
459 (Moore et al., 2017). This reduction is comparable to the reduction during the COVID-19  
460 pandemic. Our study would suggest that the adoption of more sustainable fuels, such as biofuel

461 or other synthetic fuels, in the future will increase Ni and change the microphysical properties of  
462 cirrus clouds significantly but may only lead to a small positive global average radiative effect.  
463 Our radiative forcing calculations for the effects of biofuel adoption on cirrus clouds are only  
464 indicative of these possible effects, and are based on estimates of the decrease in aircraft soot  
465 emissions together with the model estimates of the effects of these changes on Ni. The net  
466 climate effect of biofuel blending or decreased aviation would depend on the effect of all aspects  
467 (e.g. CO2 emissions decrease), which are still uncertain (Lee et al., 2021).

#### 468 **Conflict of Interest**

469 The authors declare no conflicts of interest relevant to this study.

#### 470 **Data Availability Statement**

471 The updated CESM/IMPACT model and model results used in this paper are archived  
472 online at <http://doi.org/10.5281/zenodo.5154535>.

#### 473 **References**

- 474 Adrienne, N., Budd, L., & Ison, S. (2020). Grounded aircraft: An airfield operations perspective of the challenges of  
475 resuming flights post COVID. *J Air Transp Manag*, 89, 101921.  
476 <https://www.ncbi.nlm.nih.gov/pubmed/32901184>
- 477 Airbus. (2019). Global Market Forecase: Cities, Airports & Aircraft 2019-2038.  
478 [https://www.airbus.com/content/dam/corporate-topics/strategy/global-market-forecast/GMF-2019-2038-  
479 Airbus-Commercial-Aircraft-book.pdf](https://www.airbus.com/content/dam/corporate-topics/strategy/global-market-forecast/GMF-2019-2038-Airbus-Commercial-Aircraft-book.pdf).
- 480 Barrett, S., Prather, M., Penner, J., Selkirk, H., Balasubramanian, S., Dopelheuer, A., et al. (2010). Guidance on the  
481 use of AEDT gridded aircraft emissions in atmospheric models. A technical note submitted to the US  
482 Federal Aviation Administration, Massachusetts Institute ofTechnology (MIT).
- 483 Bavel, J. J. V., Baicker, K., Boggio, P. S., Capraro, V., Cichocka, A., Cikara, M., et al. (2020). Using social and  
484 behavioural science to support COVID-19 pandemic response. *Nat Hum Behav*, 4(5), 460-471.  
485 <https://www.ncbi.nlm.nih.gov/pubmed/32355299>

486 Bogoch, I. I., Watts, A., Thomas-Bachli, A., Huber, C., Kraemer, M. U. G., & Khan, K. (2020a). Pneumonia of  
487 unknown aetiology in Wuhan, China: potential for international spread via commercial air travel. *Journal of*  
488 *Travel Medicine*, 27(2). <Go to ISI>://WOS:000531888500013

489 Bogoch, I. I., Watts, A., Thomas-Bachli, A., Huber, C., Kraemer, M. U. G., & Khan, K. (2020b). Potential for global  
490 spread of a novel coronavirus from China. *Journal of Travel Medicine*, 27(2). <Go to  
491 ISI>://WOS:000531888500014

492 Cantrell, W., & Heymsfield, A. (2005). Production of ice in tropospheric clouds: A review. *Bulletin of the American*  
493 *Meteorological Society*, 86(6), 795-808.

494 Cziczo, D. J., Murphy, D. M., Hudson, P. K., & Thomson, D. S. (2004). Single particle measurements of the  
495 chemical composition of cirrus ice residue during CRYSTAL-FACE. *Journal of Geophysical Research-*  
496 *Atmospheres*, 109(D4). <Go to ISI>://WOS:000189373600003

497 DeMott, P., Cziczo, D., Prenni, A., Murphy, D., Kreidenweis, S., Thomson, D., et al. (2003). Measurements of the  
498 concentration and composition of nuclei for cirrus formation. *Proceedings of the National Academy of*  
499 *Sciences*, 100(25), 14655-14660.

500 DeMott, P. J., Chen, Y., Kreidenweis, S. M., Rogers, D. C., & Sherman, D. E. (1999). Ice formation by black  
501 carbon particles. *Geophysical Research Letters*, 26(16), 2429-2432. <Go to  
502 ISI>://WOS:000082011200006

503 Evangeliou, N., et al. (2021), Changes in black carbon emissions over Europe due to COVID-19 lockdowns,  
504 *Atmospheric Chemistry and Physics*, 21(4), 2675-2692, doi:10.5194/acp-21-2675-5722021.

505 Forster, P. M., Forster, H. I., Evans, M. J., Gidden, M. J., Jones, C. D., Keller, C. A., et al. (2020). Current and  
506 future global climate impacts resulting from COVID-19. *Nature Climate Change*, 10(10), 913-919.

507 Garnier, A., Pelon, J., Pascal, N., Vaughan, M. A., Dubuisson, P., Yang, P., & Mitchell, D. L. (2020a). Version 4  
508 CALIPSO IIR ice and liquid water cloud microphysical properties, Part I: the retrieval algorithms.  
509 *Atmospheric Measurement Techniques Discussions*.

510 Garnier, A., Pelon, J., Pascal, N., Vaughan, M. A., Dubuisson, P., Yang, P., & Mitchell, D. L. (2020b). Version 4  
511 CALIPSO IIR ice and liquid water cloud microphysical properties, Part II: results over oceans.  
512 *Atmospheric Measurement Techniques Discussions*.

513 Gasparini, B., Blossey, P. N., Hartmann, D. L., Lin, G., & Fan, J. (2019). What Drives the Life Cycle of Tropical  
514 Anvil Clouds? *Journal of Advances in Modeling Earth Systems*, 11(8), 2586-2605. <Go to  
515 ISI>://WOS:000490949100010

516 Gasparini, B., Meyer, A., Neubauer, D., Munch, S., & Lohmann, U. (2018). Cirrus Cloud Properties as Seen by the  
517 CALIPSO Satellite and ECHAM-HAM Global Climate Model. *Journal of Climate*, 31(5), 1983-2003. <Go  
518 to ISI>://WOS:000427438100017

519 Gettelman, A., & Chen, C. (2013). The climate impact of aviation aerosols. *Geophysical Research Letters*, 40(11),  
520 2785-2789.

521 Gryspeerd, E., Sourdeval, O., Quaas, J., Delanoe, J., Kraemer, M., & Kuehne, P. (2018). Ice crystal number  
522 concentration estimates from lidar-radar satellite remote sensing – Part 2: Controls on the ice crystal

523 number concentration. *Atmospheric Chemistry and Physics*, 18(19), 14351-14370. <Go to  
524 ISI>://WOS:00044673100000

525 He, G., Pan, Y., & Tanaka, T. (2020). The short-term impacts of COVID-19 lockdown on urban air pollution in  
526 China. *Nature Sustainability*, 3(12), 1005-1011.

527 Hoose, C., & Möhler, O. (2012). Heterogeneous ice nucleation on atmospheric aerosols: a review of results from  
528 laboratory experiments. *Atmospheric Chemistry and Physics*, 12(20), 9817-9854.

529 Huang, X., Ding, A., Gao, J., Zheng, B., Zhou, D., Qi, X., et al. (2020). Enhanced secondary pollution offset  
530 reduction of primary emissions during COVID-19 lockdown in China. *National Science Review*.  
531 <https://doi.org/10.1093/nsr/nwaa137>

532 Jensen, E. J., Lawson, R. P., Bergman, J. W., Pfister, L., Bui, T. P., & Schmitt, C. G. (2013). Physical processes  
533 controlling ice concentrations in synoptically forced, midlatitude cirrus. *Journal of Geophysical Research-*  
534 *Atmospheres*, 118(11), 5348-5360. <Go to ISI>://WOS:000325212600023

535 Joos, H., Spichtinger, P., Reutter, P., & Fusina, F. (2014). Influence of heterogeneous freezing on the microphysical  
536 and radiative properties of orographic cirrus clouds. *Atmospheric Chemistry and Physics*, 14(13), 6835-  
537 6852. <Go to ISI>://WOS:000339244600022

538 Kärcher, B., Mahrt, F., & Marcolli, C. (2021). Process-oriented analysis of aircraft soot-cirrus interactions constrains  
539 the climate impact of aviation. *Communications Earth & Environment*, 2(1), 113.  
540 <https://doi.org/10.1038/s43247-021-00175-x>

541 Koop, T., Luo, B. P., Tsias, A., & Peter, T. (2000). Water activity as the determinant for homogeneous ice  
542 nucleation in aqueous solutions. *Nature*, 406(6796), 611-614. Article. <Go to  
543 ISI>://WOS:000088653800043

544 Lawson, P., Gurganus, C., Woods, S., & Brientjes, R. (2017). Aircraft Observations of Cumulus Microphysics  
545 Ranging from the Tropics to Midlatitudes: Implications for a “New” Secondary Ice Process. *Journal of*  
546 *the Atmospheric Sciences*, 74(9), 2899-2920. <Go to ISI>://WOS:000409847100010

547 Lawson, R. P., Woods, S., & Morrison, H. (2015). The Microphysics of Ice and Precipitation Development in  
548 Tropical Cumulus Clouds. *Journal of the Atmospheric Sciences*, 72(6), 2429-2445. <Go to  
549 ISI>://WOS:000355108500015

550 Le Quéré, C., Jackson, R. B., Jones, M. W., Smith, A. J. P., Abernethy, S., Andrew, R. M., et al. (2020). Temporary  
551 reduction in daily global CO2 emissions during the COVID-19 forced confinement. *Nature Climate*  
552 *Change*, 10(7), 647-653.

553 Lee, D. S., Fahey, D. W., Skowron, A., Allen, M. R., Burkhardt, U., Chen, Q., et al. (2021). The contribution of  
554 global aviation to anthropogenic climate forcing for 2000 to 2018. *Atmos Environ* (1994), 244, 117834.  
555 <https://www.ncbi.nlm.nih.gov/pubmed/32895604>

556 Mahrt, F., Kilchhofer, K., Marcolli, C., Grönquist, P., David, R. O., Rösch, M., et al. (2019). The Impact of Cloud  
557 Processing on the Ice Nucleation Abilities of Soot Particles at Cirrus Temperatures. *Journal of Geophysical*  
558 *Research: Atmospheres*.



559 Mahrt, F., Kilchhofer, K., Marcolli, C., Grönquist, P., David, R. O., Rösch, M., et al. (2020). The Impact of Cloud  
560 Processing on the Ice Nucleation Abilities of Soot Particles at Cirrus Temperatures. *Journal of Geophysical*  
561 *Research: Atmospheres*, 125(3).

562 Mitchell, D. L., Garnier, A., Pelon, J., & Erfani, E. (2018). CALIPSO (IIR-CALIOP) retrievals of cirrus cloud ice-  
563 particle concentrations. *Atmospheric Chemistry and Physics*, 18(23), 17325-17354. <Go to  
564 ISI>://WOS:000452383600005

565 Mohler, O., Buttner, S., Linke, C., Schnaiter, M., Saathoff, H., Stetzer, O., et al. (2005). Effect of sulfuric acid  
566 coating on heterogeneous ice nucleation by soot aerosol particles. *Journal of Geophysical Research-*  
567 *Atmospheres*, 110(D11). <Go to ISI>://WOS:000229988800002

568 Moore, R. H., Thornhill, K. L., Weinzierl, B., Sauer, D., D'Ascoli, E., Kim, J., et al. (2017). Biofuel blending  
569 reduces particle emissions from aircraft engines at cruise conditions. *Nature*, 543(7645), 411-415.  
570 <https://www.ncbi.nlm.nih.gov/pubmed/28300096>

571 Penner, J. E., Zhou, C., Garnier, A., & Mitchell, D. L. (2018). Anthropogenic Aerosol Indirect Effects in  
572 Cirrus Clouds. *Journal of Geophysical Research: Atmospheres*, 123(20), 11, 652-611,677.

573 Phillips, C. A., Caldas, A., Cleetus, R., Dahl, K. A., Declet-Barreto, J., Licker, R., et al. (2020). Compound climate  
574 risks in the COVID-19 pandemic. *Nature Climate Change*, 10(7), 586-588.

575 Pitari, G., Iachetti, D., Di Genova, G., De Luca, N., Sovde, O. A., Hodnebrog, O., et al. (2015). Impact of Coupled  
576 NO<sub>x</sub>/Aerosol Aircraft Emissions on Ozone Photochemistry and Radiative Forcing. *Atmosphere*, 6(6), 751-  
577 782. <Go to ISI>://WOS:000357152500002

578 Richardson, M. S., DeMott, P. J., Kreidenweis, S. M., Cziczo, D. J., Dunlea, E. J., Jimenez, J. L., et al. (2007).  
579 Measurements of heterogeneous ice nuclei in the western United States in springtime and their relation to  
580 aerosol characteristics. *Journal of Geophysical Research-Atmospheres*, 112(D2). <Go to  
581 ISI>://WOS:000244041400002

582 Righi, M., Hendricks, J., & Beer, C. G. (2021). Exploring the uncertainties in the aviation soot-cirrus effect. *Atmos.*  
583 *Chem. Phys. Discuss.*, 2021, 1-31. <https://acp.copernicus.org/preprints/acp-2021-329/>

584 Samset, B. H., et al. (2014), Modelled black carbon radiative forcing and atmospheric lifetime in AeroCom Phase II  
585 constrained by aircraft observations, *Atmospheric Chemistry and Physics*, 14(22), 12465-12477,  
586 doi:10.5194/acp-14-12465-2014.

587 SABRE. (2020). Market intelligence global demand data,  
588 [http://www.sabreairlinesolutions.com/home/software\\_solutions/airports/](http://www.sabreairlinesolutions.com/home/software_solutions/airports/).

589 Schumann, U., Poll, I., Teoh, R., Koelle, R., Spinielli, E., Molloy, J., et al. (2021). Air traffic and contrail changes  
590 over Europe during COVID-19: a model study. *Atmospheric Chemistry and Physics*, 21(10), 7429-7450.  
591 <Go to ISI>://WOS:000653621700001

592 Sourdeval, O., Gryspeerdt, E., Kraemer, M., Goren, T., Delanoe, J., Afchine, A., et al. (2018). Ice crystal number  
593 concentration estimates from lidar-radar satellite remote sensing – Part 1: Method and evaluation.  
594 *Atmospheric Chemistry and Physics*, 18(19), 14327-14350. <Go to ISI>://WOS:000446731000004

595 Ström, J., & Ohlsson, S. (1998). In situ measurements of enhanced crystal number densities in cirrus clouds caused  
596 by aircraft exhaust. *Journal of Geophysical Research: Atmospheres*, 103(D10), 11355-11361.

597 Tesche, M., Achtert, P., Glantz, P., & Noone, K. J. (2016). Aviation effects on already-existing cirrus clouds. *Nat*  
598 *Commun*, 7, 12016. <https://www.ncbi.nlm.nih.gov/pubmed/27327838>

599 Urbanek, B., Groß, S., Wirth, M., Rolf, C., Krämer, M., & Voigt, C. (2018). High depolarization ratios of naturally  
600 occurring cirrus clouds near air traffic regions over Europe. *Geophysical Research Letters*, 45(23), 13,166-  
601 113,172.

602 Venter, Z. S., Aunan, K., Chowdhury, S., & Lelieveld, J. (2020). COVID-19 lockdowns cause global air pollution  
603 declines. *Proc Natl Acad Sci U S A*, 117(32), 18984-18990.  
604 <https://www.ncbi.nlm.nih.gov/pubmed/32723816>

605 Wang, B., Lambe, A. T., Massoli, P., Onasch, T. B., Davidovits, P., Worsnop, D. R., & Knopf, D. A. (2012). The  
606 deposition ice nucleation and immersion freezing potential of amorphous secondary organic aerosol:  
607 Pathways for ice and mixed-phase cloud formation. *Journal of Geophysical Research: Atmospheres*,  
608 117(D16).

609 Wilkerson, J. T., Jacobson, M. Z., Malwitz, A., Balasubramanian, S., Wayson, R., Fleming, G., et al. (2010).  
610 Analysis of emission data from global commercial aviation: 2004 and 2006. *Atmospheric Chemistry and*  
611 *Physics*, 10(13), 6391-6408. <Go to ISI>://WOS:000279851400043

612 Worldometers. (2021). Coronavirus Cases. Retrieved 25.10.2021, from  
613 <https://www.worldometers.info/coronavirus/>.

614 Yang, Y., Ren, L., Li, H., Wang, H., Wang, P., Chen, L., et al. (2020). Fast Climate Responses to Aerosol Emission  
615 Reductions During the COVID-19 Pandemic. *Geophysical Research Letters*, 47(19).

616 Zhao, B., Wang, Y., Gu, Y., Liou, K. N., Jiang, J. H., Fan, J., et al. (2019). Ice nucleation by aerosols from  
617 anthropogenic pollution. *Nat Geosci*, 12, 602-607. <https://www.ncbi.nlm.nih.gov/pubmed/31360220>

618 Zheng, B., Zhang, Q., Geng, G., Chen, C., Shi, Q., Cui, M. et al. (2021). Changes in China's anthropogenic  
619 emissions and air quality during the COVID-19 pandemic in 2020, *Earth Syst. Sci. Data*, 13, 2895–2907,  
620 <https://doi.org/10.5194/essd-13-2895-2021>.

621 Zhou, C., & Penner, J. E. (2014). Aircraft soot indirect effect on large-scale cirrus clouds: Is the indirect forcing by  
622 aircraft soot positive or negative? *Journal of Geophysical Research-Atmospheres*, 119(19), 11303-11320.  
623 Article. <Go to ISI>://WOS:000344053400020

624 Zhu, J., & Penner, J. E. (2019). Global Modeling of Secondary Organic Aerosol With Organic Nucleation. *Journal*  
625 *of Geophysical Research: Atmospheres*, 124(14), 8260-8286.

626 Zhu, J., & Penner, J. E. (2020a). Indirect Effects of Secondary Organic Aerosol on Cirrus Clouds. *Journal of*  
627 *Geophysical Research: Atmospheres*, 125(7).

628 Zhu, J., & Penner, J. E. (2020b). Radiative forcing of anthropogenic aerosols on cirrus clouds using a hybrid ice  
629 nucleation scheme. *Atmospheric Chemistry and Physics*, 20(13), 7801-7827.

630 Zhu, J., Penner, J. E., Lin, G., Zhou, C., Xu, L., & Zhuang, B. (2017). Mechanism of SOA formation determines  
631 magnitude of radiative effects. *Proc Natl Acad Sci U S A*, 114(48), 12685-12690.  
632 <https://www.ncbi.nlm.nih.gov/pubmed/29133426>  
633 Zhu, J., Penner, J. E., Yu, F., Sillman, S., Andreae, M. O., & Coe, H. (2019). Decrease in radiative forcing by  
634 organic aerosol nucleation, climate, and land use change. *Nature Communications*, 10(1), 423.  
635 <https://doi.org/10.1038/s41467-019-08407-7>  
636  
637

638 **Table 1.** Difference in the median and average Ni ( $L^{-1}$ ) between 2019 and 2018, 2020 and 2019,  
 639 and 2020 and 2019 as well as the difference between 2020 and the average of 2019 and 2018 and  
 640 between 2020 and the average of 2010-2019 as measured by CALIPSO.

641

		2019-2018	2020-2018	2020-2019	2020-AVE1*	2020-AVE2#	
Jan-Feb	60°S-60°N	3.44	-1.59	-5.04	-3.32	-	
	Median	30°N-60°N	19.31	-5.37	-24.68	-15.02	-
		0°-30°N	-2.56	-2.93	-0.38	-1.66	-
		30°S-0°	0.52	2.72	2.19	2.45	-
	60°S-30°S	-4.00	-0.08	3.92	<b>1.92</b>	-	
	60°S-60°N	3.26	-2.61	-5.87	-4.24	-	
	Average	30°N-60°N	22.68	6.19	-16.49	-5.15	-
		0°-30°N	7.69	-6.86	-14.55	-10.7	-
		30°S-0°	-4.45	-9.95	-5.51	-7.73	-
		60°S-30°S	-12.88	0.19	13.08	6.64	-
60°S-60°N		-1.28	13.95	<b>15.23</b>	<b>14.59</b>	<b>12.74</b>	
Apr-May	Median	30°N-60°N	9.70	<b>36.24</b>	26.54	<b>31.39</b>	<b>24.21</b>
		0°-30°N	9.93	15.55	5.61	10.58	<b>9.07</b>
		30°S-0°	-7.03	-4.60	2.43	-1.09	4.69
	60°S-30°S	-18.89	7.85	26.74	17.30	<b>11.63</b>	
	60°S-60°N	3.00	<b>20.01</b>	<b>17.01</b>	<b>18.51</b>	<b>14.34</b>	
	Average	30°N-60°N	7.45	<b>42.15</b>	<b>34.71</b>	<b>38.43</b>	<b>29.68</b>
		0°-30°N	<b>22.06</b>	<b>25.41</b>	3.35	<b>14.38</b>	<b>12.06</b>
		30°S-0°	40.43	40.45	0.01	4.19	6.56
60°S-30°S		-24.45	5.53	29.98	17.76	7.75	

642 Note: Italicized and bold numbers are statistically significant at the 95% level according to a Student's t test for the  
 643 averages and a Mood's test for the medians.

644 \*AVE1 stands for the average of Ni in 2018 and 2019.

645 #AVE2 stands for the average of Ni from 2010 to 2019.

646

647

648 Figure 1. The number concentration of ice crystal (Ni) from CALIPSO observations in the  
649 latitude bands of 30°N~30°N, 0~30°N, 30°S~0, and 60°S~30°N. Panel A: the comparison of  
650 median and average Ni in January-February between 2018, 2019 and 2020. Panel B: the  
651 comparison of median and average Ni in April-May between 2018, 2019 and 2020. Panel C: The  
652 median as well as 25<sup>th</sup> and 27<sup>th</sup> percentile detrended Ni anomaly ( $L^{-1}$ ) in April and May from  
653 2010 to 2020. The dotted black box indicates a region where Ni in April-May of 2020 is  
654 evidently higher relative to Ni for 2018 and 2019.

655

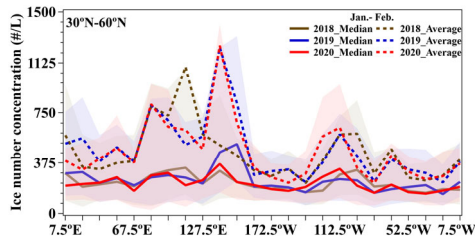
656 Figure 2. The comparison between observed (blue line) and simulated (red line) median (solid  
657 line) and average (dashed line) ice number concentration ( $L^{-1}$ ) in cirrus clouds for 30°N~60°N  
658 (a), 0~30°N (b), 30°S~0 (c), and 60°S~30°S (d) during January-May from 2018 to 2020. The  
659 shading represents the 25<sup>th</sup> and 75<sup>th</sup> percentiles of the median.

660

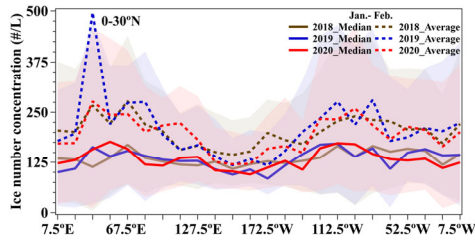
661 Figure 3. The change in the annual average vertically integrated number concentration ( $m^{-2}$ ) of  
662 total ice crystals (a) and all-sky net radiative effect ( $W m^{-2}$ ) (c) due to a flight decrease for five  
663 years. Differences significant at the 95% level according to a Student's t test in (a) and (c) are  
664 depicted by points. The change in the annual average vertically integrated number concentration  
665 of total ice (b, red solid line), ice from homogenous freezing (b, orange dashed line), and ice  
666 from heterogeneous freezing (b, blue dashed line) versus latitude due to the reduction in aircraft  
667 flights for five years. The change in all-sky longwave radiative effect (d, orange dashed line), all-  
668 sky shortwave radiative effect (d, blue dashed line), and all-sky net radiative effect (d, solid red  
669 line) versus latitude due to a reduction in aircraft flights for five years. All plots are the  
670 difference between cases EX\_L2 and EX\_L1 (See method section). The shading in (b) and (d)  
671 represents 1 standard deviation of the interannual variation of the column number concentration  
672 and net radiative effect, respectively, over five years. Significant differences between (b) and (d)  
673 and the 95% level according to a Student's t test are depicted by grey shading.

# Panel A January/February

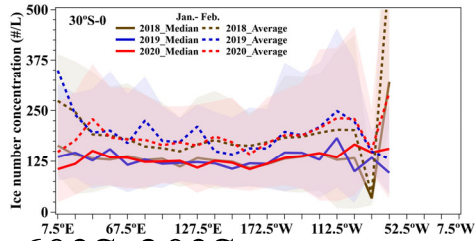
## 30°N-60°N



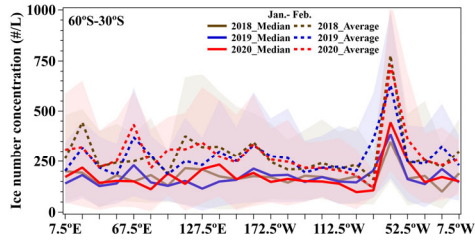
## 0°-30°N



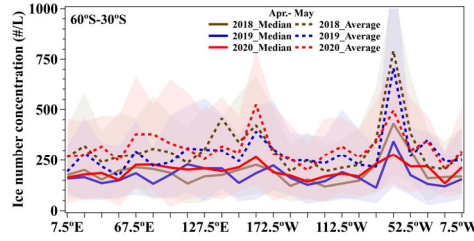
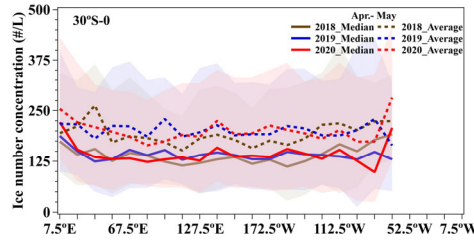
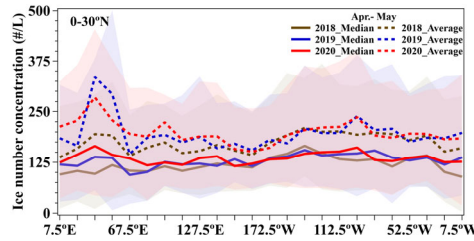
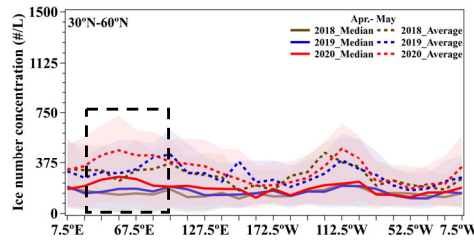
## 30°S-0°



## 60°S-30°S



# Panel B April/May



# Panel C 11 years

